nature communications

Article

https://doi.org/10.1038/s41467-025-60153-1

Reaction-induced dynamic evolution of PtIn/SiO_2 catalyst for propane dehydrogenation

Received: 20 October 2024

Accepted: 14 May 2025

Published online: 03 June 2025

Check for updates

Tao Zhou[1,7], Han Yan[1,7], Wenjie Li[2], Wenjian Zhang[1], Hongtao He[1], Sunpei Hu[1], Ruyang Wang[2], Tianci Xiao[2], Limin Liu[2], Lijun Zhang[3], Wenlong Wu[3], Chengyuan Liu[2], Xusheng Zheng[2], Yang Pan[2], Jie Zeng[1,3,4,5] ✉ & Xu Li[1,6] ✉

Understanding the dynamic evolution of heterogeneous catalysts is crucial yet challenging for elucidating the structure-performance relationships and enabling rational catalyst design. Herein, we reveal that PtIn alloy clusters gradually evolve into Pt_3In intermetallic in response to propylene, the product of propane dehydrogenation (PDH) reaction. Specifically, a $PtIn_{1.0}/SiO_2$ catalyst has been fabricated, comprising sub-nanometric PtIn alloy clusters covered by an In^0 overlayer, with In^{3+} species locating at the metal-support interface. During the PDH reaction propylene induces the evaporation of the In^0 overlayer, thereby exposing Pt sites. After an induction period, the evolved Pt_3In intermetallic (average size ~1.3 nm) exhibits a C_3H_6 productivity of 145 mol g_{Pt}^{-1} h^{-1}. The alloyed In^0 species effectively dilute Pt-Pt ensembles, enhancing propylene selectivity, while the interfacial In^{3+} species inhibit aggregation of Pt_3In intermetallic, ensuring excellent catalytic stability. These findings underscore the critical role of product molecules in shaping active site evolution at the atomic scale.

The critical role of heterogeneous catalysts in facilitating chemical production and energy conversion processes cannot be overstated[1–3]. These catalysts, typically composed of active metals dispersed on support, are subject to a continuous process of dynamic evolution during operation[4,5]. Affected by the reaction environment, including temperature and atmosphere, the structural and chemical properties of catalysts are strongly altered[6]. Elevated temperatures promote the atomic rearrangement of active metals and supports, leading to phenomena such as sintering, redispersion, and facet restructuring[7–10]. In addition, the coordination of reactant or product molecules on metal surfaces significantly alters the surface energy, thus changing their structure and chemical properties[11–14]. For alloy catalysts, the structural diversity stemming from various distributions and proportions of components results in a richer dynamic evolution. Numerous gas molecules, including CO, NO, and O_2, have been demonstrated to induce the element segregation and even composition changes of alloy[11,13,15]. This dynamic evolution of the catalyst results in dramatic changes in catalytic performance, which is an overlooked factor in studying the structure-performance relationship[16]. Therefore, an unambiguous understanding of the catalyst dynamics is crucial for the identification of the real active sites and the rational design of high-performance heterogeneous catalysts.

On-purpose propane dehydrogenation (PDH) technologies (ΔH_{298K} = 124.3 kJ mol^{-1}) have drawn intensive attention in recent years,

[1]Hefei National Research Center for Physical Sciences at the Microscale, University of Science and Technology of China, Hefei, Anhui, P. R. China. [2]National Synchrotron Radiation Laboratory, University of Science and Technology of China, Hefei, Anhui, P. R. China. [3]School of Chemistry & Chemical Engineering, Anhui University of Technology, Ma'anshan, Anhui, P. R. China. [4]Key Laboratory of Strongly-Coupled Quantum Matter Physics of Chinese Academy of Sciences, University of Science and Technology of China, Hefei, Anhui, P. R. China. [5]Key Laboratory of Surface and Interface Chemistry and Energy Catalysis of Anhui Higher Education Institutes, Department of Chemical Physics, University of Science and Technology of China, Hefei, Anhui, P. R. China. [6]School of Materials and Energy, University of Electronic Science and Technology of China, Chengdu, P. R. China. [7]These authors contributed equally: Tao Zhou, Han Yan. ✉e-mail: zengj@ustc.edu.cn; xuli@uestc.edu.cn

driven by the ever-increasing market demands for propylene and the revolution of shale gas feedstocks[17]. The research emphasis of high-performance PDH catalysts focuses on the fabrication of highly-dispersed Pt-M alloy, where M represents promoters, including In[18–20], Sn[21–23], Cu[24,25], Ga[26], Zn[27–29], and so on[30–34]. The addition of catalytic-inert elements is reported to dilute Pt-Pt ensembles, thus improving propylene selectivity[35]. Meanwhile, richer structural evolution also appeared due to the introduction of promoters. In the PDH reaction, high temperature and reductive atmosphere, especially H_2, are widely recognized as key drivers of structural evolution in Pt-M alloy catalysts[36]. However, to the best of our knowledge, the dynamic evolution of Pt-M alloys induced by propylene, the target product of PDH reaction, has not been reported. Revealing the interaction between propylene and metal sites is expected to provide a deeper understanding of this reaction and guide the rational design of PDH catalysts.

Herein, we report the dynamic evolution of the sub-nanometric PtIn clusters into ultrafine Pt_3In intermetallics, driven by the propylene molecules. Upon H_2 reduction, PtIn alloy clusters covered by In^0 overlayer were formed, while dominant In^{3+} species were still presented on the PtIn-SiO_2 interface and surface of the support. During the PDH reaction, propylene was found to induce the evaporation of the In^0 overlayer, markedly enhancing catalytic activity. Moreover, the remained In^0 species effectively diluted Pt sites to improve propylene selectivity, while In^{3+} species at the Pt_3In-SiO_2 interface inhibited the aggregation of Pt_3In intermetallic clusters. As a result, the evolved Pt_3In intermetallics (average size ~1.3 nm) exhibited a C_3H_6 selectivity of 97% and a productivity of 145 mol g_{Pt}^{-1} h^{-1}, which was an order of magnitude higher than previously reported PtIn-based catalysts. These results highlight the pivotal role of product molecules in governing structure-performance relationships and identifying the true active sites.

Results

Preparation and characterization of PtIn catalysts

The catalyst was fabricated using a stepwise strong electrostatic adsorption (SEA) method. First, SiO_2 was immersed in an alkaline solution to impart a negative surface charge since the pH was higher than its point of zero charge (PZC = 2.8)[37]. To avoid the formation of $In(OH)_3$ precipitation in the next step, excess OH^- ions were removed by washing SiO_2 with deionized water. The treated SiO_2 was then re-dispersed in water, and In^{3+} cations were adsorbed on the negatively-charged SiO_2 surface. The nominal loading of In was 1.0 wt% relative to SiO_2, and the resulting powder was dried and calcined at 300 °C for 1 h, named $In_{1.0}/SiO_2$. Next, $Pt(NH_3)_4^{2+}$ cations were adsorbed onto $In_{1.0}/SiO_2$ by controlling the pH to 9 − 10, and the resulting powder was reduced at 600 °C with H_2 for 1 h, named $PtIn_{1.0}/SiO_2$. Compared with the impregnation method, such a SEA technique ensures a uniform distribution of Pt and In on SiO_2 with low metal loading (< 1 wt%)[38]. The actual Pt and In loadings were determined to be 0.12 wt% and 0.90 wt% by inductively coupled plasma-mass spectroscopy (ICP-MS), respectively. A series of $PtIn_x/SiO_2$ catalysts with fixed Pt loading but varying In loadings was further synthesized to elucidate the effect of In loading on catalytic performance. For comparison, Pt/SiO_2 was synthesized by directly adsorbing $Pt(NH_3)_4^{2+}$ cations onto SiO_2. In addition, SiO_2-supported Pt_3In intermetallic nanoparticles (Pt_3In NPs/SiO_2) were synthesized following the procedure in literature[39]. The nominal Pt-to-In mass ratio, along with values obtain from ICP-MS and X-ray photoelectron spectroscopy (XPS) are presented in Supplementary Table 1.

The *quasi* in situ X-ray absorption near-edge structure (XANES) and extended X-ray absorption fine structure (EXAFS) spectra were measured to determine the electronic structures of Pt/SiO_2 and $PtIn_{1.0}/SiO_2$. As shown in Fig. 1a, the absorption energies of both Pt/SiO_2 and $PtIn_{1.0}/SiO_2$ were close to Pt foil, indicating a metallic state.

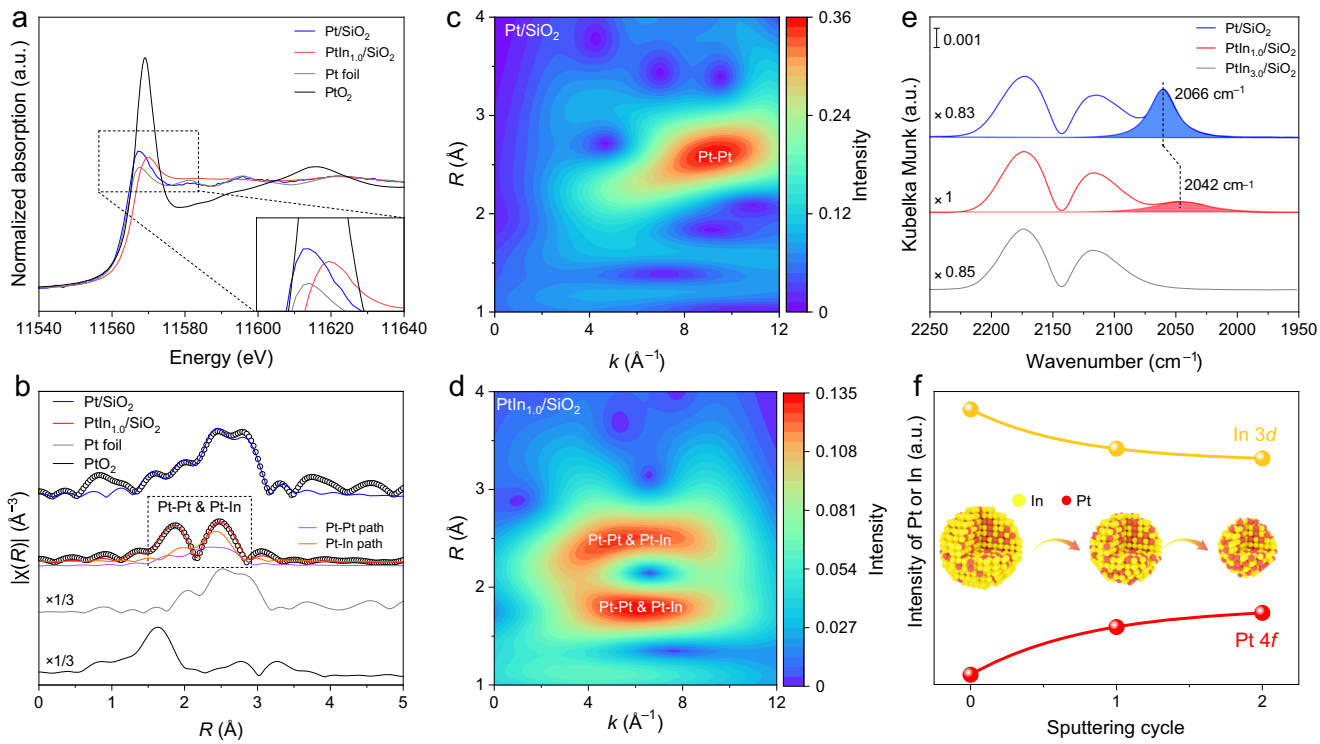

Fig. 1 | Electronic and coordination structure of PtIn alloy. a, **b** XANES (**a**) and EXAFS (**b**) spectra at the Pt L_{III}-edge of Pt/SiO_2, $PtIn_{1.0}/SiO_2$, Pt foil, and PtO_2. **c**, **d** The wavelet transformed EXAFS of Pt/SiO_2 (**c**) and $PtIn_{1.0}/SiO_2$ (**d**). **e** CO DRIFTS results of Pt/SiO_2, $PtIn_{1.0}/SiO_2$, and $PtIn_{3.0}/SiO_2$. a.u., arbitrary units. **f** Changes of Pt 4*f* and In 3*d* intensities in XPS spectra during the sputtering cycles.

Notably, compared with Pt/SiO_2, $PtIn_{1.0}/SiO_2$ exhibited an obvious decrease in white line intensity but an increase in the absorption energy. According to previous studies, the Pt-L_{III} edge represents the dipole transitions from the $2p_{3/2}$ orbital to the unoccupied $5d_{5/2}$ orbital. Thus, the variations in white line intensity reflect changes in the unoccupied $5d_{5/2}$ orbital, such as those induced by alloy or oxidation[40]. The formation of PtIn alloy is reported to result in the charge transfer from In 5*p* to Pt 5*d* orbital, thereby reducing the proportion of unoccupied Pt 5*d* orbital[39]. Thus, the decreased white line intensity of the Pt-L_{III} edge reflects the electron redispersion between Pt and In caused by the formation of PtIn alloy. Meanwhile, the higher absorption energy of $PtIn_{1.0}/SiO_2$ was also caused by the accumulation of electrons on Pt[41].

The coordination structure of $PtIn_{1.0}/SiO_2$ was investigated by EXAFS spectra (Fig. 1b–d and Supplementary Table 2). The Pt/SiO_2 sample showed a Pt–Pt coordination number (CN) of 5.9 at a bonding distance of 2.79 Å and a low Pt–O CN (0.5) at a bonding distance of 2.02 Å. For $PtIn_{1.0}/SiO_2$, a Pt–Pt CN of 2.2 and a Pt–In CN of 2.6 were fitted, suggesting the formation of PtIn alloy[42]. Compared to that of Pt/SiO_2, the bonding distance of Pt–Pt and Pt–In was reduced to 2.55 Å and 2.56 Å, respectively. It has been reported that transitioning from bulk to small metal nanoparticles (NPs) leads to the de-hybridization of metal orbitals and a contraction in bonding distances[41]. Thus, the reduced bonding distance implied the small size of the PtIn alloy. In addition, XAFS measurements at the In *K*-edge were also measured to determine the electronic environment of In species (Supplementary Fig. 1 and Table 2). Compared to $In_{1.0}/SiO_2$, $PtIn_{1.0}/SiO_2$ exhibited a decreased absorption energy and white line intensity, indicating a lower oxidation state. EXAFS fitting results showed a CN of 5.9 for In–O in $In_{1.0}/SiO_2$, highly close to a saturated In–O CN (6.0) in bulk In_2O_3. The high CN of In–O in $In_{1.0}/SiO_2$ suggested that In^{3+} species were dominant in the reduced samples. In contrast, $PtIn_{1.0}/SiO_2$ showed a lower In–O CN of 4.4, indicating that the In^{3+} species were partially reduced upon the addition of Pt.

To further investigate the reduction degree of Pt and In, H_2 temperature-programmed reduction (TPR) experiments were performed. As illustrated in Supplementary Fig. 2, the Pt/SiO_2 sample exhibited a distinct reduction peak at 303 °C, corresponding to the reduction of Pt^{2+} species. In^{3+} species in $In_{1.0}/SiO_2$ were reduced at 550 °C. For $PtIn_{1.0}/SiO_2$, a more pronounced reduction peak of In^{3+} species was observed, along with an additional peak at 505 °C. This peak was attributed to the reduction of In^{3+} species facilitated by Pt^0. By assuming the complete reduction of Pt^{2+}, we calculated the percentage of In^0 species based on H_2 consumption. For $In_{1.0}/SiO_2$, only 0.8% of In^{3+} was reduced to a metallic state. Upon Pt loading, the In^0 content increased to 2.8%, indicating that Pt^0 promoted the reduction of In^{3+} species. Nevertheless, the majority of In remained in the oxidized state as In^{3+} (97.2%). For $PtIn_{1.0}/SiO_2$, the atomic ratio of Pt^0 to In^0 was calculated as 1 / 0.4. EXAFS fitting results further exhibited comparable CNs for Pt-Pt and Pt-In, suggesting that Pt^0 species were coordinated with both alloyed In^0 species and oxidized In^{3+} species. In other words, in PtIn clusters, In^{3+} species were present at the interface between the PtIn alloy and SiO_2 support.

CO probe diffuse reflectance infrared Fourier transform spectroscopy (DRIFTS) was employed to explore the surface geometry configuration of Pt. As depicted in Fig. 1e and Supplementary Fig. 3, Pt/SiO_2 exhibited a peak at 2,066 cm^{-1}, corresponding to the stretching vibration of linearly adsorbed CO on Pt sites. For $PtIn_{1.0}/SiO_2$, the CO adsorption peak exhibited a red shift to 2042 cm^{-1} owing to the electron accumulation on metallic Pt sites. Consistent with the XANES results, CO DRIFTS measurements indicate the electron transfer from In to Pt. Moreover, the integral intensity of the CO adsorption peaks markedly decreased for $PtIn_{1.0}/SiO_2$, and completely vanished for $PtIn_{3.0}/SiO_2$ with a higher In loading. Thus, we deduce that an In^0 overlayer was present on the surface of the PtIn alloy, likely driven by the difference in surface energy between Pt and In. In general, elements with lower surface energy tend to segregate to the surface of an alloy to minimize the overall system energy[43,44].

The valence states of Pt and In were investigated using *quasi* in situ XPS. The binding energies of Pt 4*f* in Pt/SiO_2 and $PtIn_{1.0}/SiO_2$ were centered at 71.6 and 71.4 eV, respectively, suggesting a metallic state of Pt[19]. The 0.2 eV downshift in the binding energy of $PtIn_{1.0}/SiO_2$ indicated the charge transfer from In to Pt (Supplementary Fig. 4a). The XPS results for In 3*d* are shown in Supplementary Fig. 4b. Both $In_{1.0}/SiO_2$ and $PtIn_{1.0}/SiO_2$ exhibited a peak centered at 445.2 eV, attributed to dominant In^{3+} species. The minor In^0 species were challenging to detect by XPS. To further investigate the distribution of Pt and In atoms in PtIn alloy, XPS analysis with Ar^+ sputtering was performed. In this case, Pt_2In_{10}/SiO_2 with a Pt loading of 1.3 wt% and a In loading of 10.8 wt% was used to improve the signal-to-noise ratio of XPS spectra (Fig. 1f, Supplementary Table 1 and Fig. 5). With increasing sputtering cycles, the In signal intensity gradually decreased while the Pt signal intensity increased. Thus, we conclude that an In^0 overlayer exists on the surface of the PtIn alloy.

The structural characteristics of Pt and In after H_2 reduction at 600 °C were investigated using electron microscopy. As shown in Supplementary Fig. 6, high-angle annular dark-field scanning transmission electron microscopy (HAADF-STEM) images revealed that Pt NPs in Pt/SiO_2 were randomly distributed with an average size of 2.5 nm. The presence of particles up to 6 nm indicated that Pt NPs on SiO_2 underwent sintering during H_2 reduction. In comparison, the PtIn alloy in $PtIn_{1.0}/SiO_2$ was uniformly dispersed on SiO_2 with an average size of 0.9 nm, showcasing the enhanced sintering resistance of $PtIn_{1.0}/SiO_2$ (Fig. 2a). EDX elemental mapping images indicated that the signal of Pt and In was homogeneously distributed across the surface of SiO_2, also suggesting the small and well-dispersed nature of PtIn alloy (Fig. 2b). It has been reported that these unreduced metal species at the interface between NPs and support, called oxide nano-islands, play a key role in frustrating the aggregation of metal NPs[45]. On one hand, compared to In^0 species, these unreduced In^{3+} species bonded with SiO_2 more tightly through Si-O-In bonding[39]. On the other hand, In^{3+} species exhibited better stabilization effect on Pt^0 species than pure SiO_2 does[18]. Thus, these In^{3+} species at the interface between PtIn clusters and SiO_2 support effectively improve the sintering resistance of PtIn clusters.

The atomically resolved HAADF-STEM characterizations were performed to reveal the configuration and composition of the PtIn alloy. As shown in Supplementary Fig. 7, Pt/SiO_2 exhibited well-crystallized Pt NPs with distinct lattice fringes. In contrast, $PtIn_{1.0}/SiO_2$ exhibited substantial single atoms and clusters, which were identified as atomically dispersed In^{3+} species and PtIn clusters, respectively (Supplementary Fig. 8). The structure of individual PtIn clusters was further analyzed based on the brightness of these spots. The 3D intensity distribution map derived from HAADF-STEM image defined the brightness of atomically dispersed In^{3+} species and PtIn clusters (Fig. 2c, d, and Supplementary Fig. 9). In PtIn clusters, most of the spots were identified as In atoms, while these spots with greater brightness were assumed to be a combination of Pt and In atoms. To validate this structural interpretation, we constructed an atomic-scale model of SiO_2-supported PtIn cluster and performed HAADF-STEM image simulations using QSTEM software (Fig. 2e). Consequently, the 3D intensity distribution map derived from the simulated HAADF-STEM image was in well accordance with the experimental results (Fig. 2c and Supplementary Fig. 10). Thus, the structure of the individual PtIn cluster was elucidated at an atomic scale, in which Pt atoms were covered by In atoms (Fig. 2f). This atomic-scale structural elucidation provides critical insights into the surface composition and coordination environment of the bimetallic system.

https://doi.org/10.1038/s41467-025-60153-1

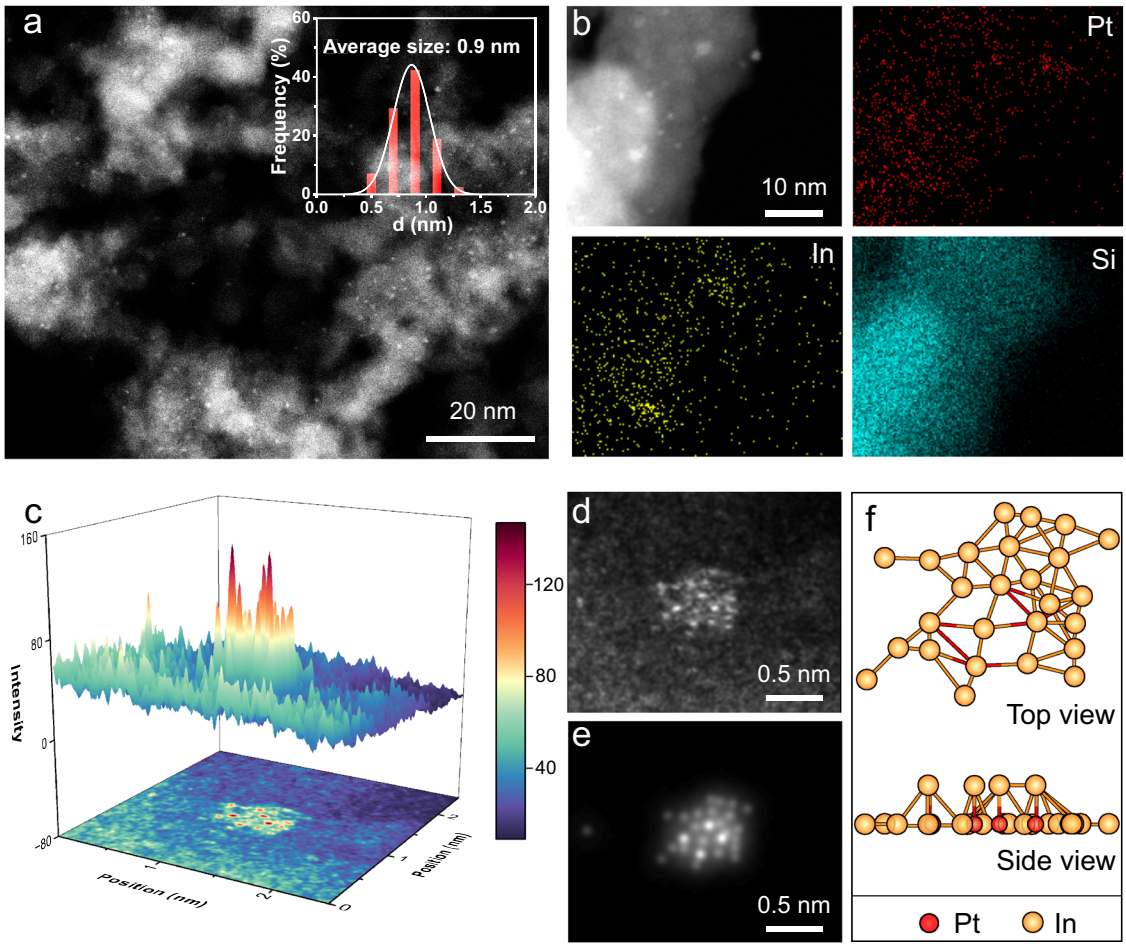

Fig. 2 | Microscopic structure characterizations. a HAADF-STEM image and corresponding size distribution of $PtIn_{1.0}/SiO_2$. **b** HAADF-STEM image and EDX elemental mapping images of $PtIn_{1.0}/SiO_2$. **c**, **d** 3D intensity distribution map and HAADF-STEM image of an individual cluster. **e**, **f** Simulated HAADF-STEM image and proposed model of the above cluster.

Catalytic performance towards PDH reaction

From an economic perspective in industrial production, enhancing the conversion efficiency of reactants per unit mass of catalyst is significantly advantageous. This can be strategically achieved by elevating the concentration of the reactants involved. Whereas, in PDH reaction, excessively high partial pressure of propane results in the coke formation, thus placing high demands on the stability of catalysts[46]. Generally, high propane (C_3H_8) and propylene (C_3H_6) partial pressures favor coke formation, while high hydrogen (H_2) partial pressure is reported to mitigate it[47]. We first evaluated the PDH catalytic performance under a relatively mild condition (550 °C, 10% C_3H_8 diluted in Ar). As shown in Supplementary Fig. 11a, the $PtIn_{1.0}/SiO_2$ catalyst exhibited poor catalytic performance. During the 30 h time on stream (TOS), C_3H_8 conversion dropped rapidly from 16.8% to 11.3%. The initial C_3H_6 productivity was calculated as 18 mol g_{Pt}^{-1} h^{-1} (Fig. 3a). To quantify deactivation of the catalyst, we calculated the mean lifetime based on an overall first-order deactivation mechanism[31,48]:

$$\tau = t/\{[\ln[(1-X_{C3H8,\,final})/X_{C3H8,\,final}] - \ln[(1-X_{C3H8,\,initial})/X_{C3H8,\,initial}]\} \quad (1)$$

where $X_{C3H8,\,final}$, $X_{C3H8,\,initial}$, and t represent the final C_3H_8 conversion, initial C_3H_8 conversion, and reaction time, respectively. $PtIn_{1.0}/SiO_2$ gave a mean lifetime of 68 h. When the C_3H_8 partial pressure was over 40%, an unexpected induction period was observed. The C_3H_8 conversion continuously increased to reach a maximum and then slightly dropped as the PDH reaction proceeded (Supplementary Fig. 11b–d). Besides, $PtIn_{1.0}/SiO_2$ exhibited higher mean lifetime values when the partial pressure of C_3H_8 exceeded 40% (Supplementary Fig. 12). Notably, the C_3H_6 productivity reached as high as 197 mol g_{Pt}^{-1} h^{-1} under pure C_3H_8, which was 11 times higher than that under 10% C_3H_8 (Fig. 3a). In short, high C_3H_8 partial pressures are beneficial for achieving high PDH catalytic activity and stability of $PtIn_{1.0}/SiO_2$ catalyst.

To further unveil the relationship between the induction period and the In loading, a series of $PtIn_x/SiO_2$ catalysts with different Pt-to-In mass ratios was prepared and evaluated (Fig. 3b and Supplementary Fig. 13). We co-fed H_2 with C_3H_8 to lower the coverage of deeply dehydrogenated coke precursors, thus mitigating coke formation. The following PDH tests were operated at 550 °C with the weight hourly space velocity (WHSV) of 39 h^{-1} (C_3H_8/H_2 = 2/1). For $PtIn_{0.2}/SiO_2$ and $PtIn_{0.4}/SiO_2$, the induction period was absent. C_3H_8 conversion and C_3H_6 selectivity decreased constantly during the 20-h TOS. The mean lifetime of $PtIn_{0.2}/SiO_2$ and $PtIn_{0.4}/SiO_2$ was calculated to be 19 h and 48 h, respectively. When In loading was further increased to 0.6 wt%, C_3H_8 conversion increased to a maximum and then gradually dropped over a 20-h TOS. $PtIn_{0.6}/SiO_2$ and $PtIn_{0.8}/SiO_2$ exhibited induction periods of 10.7 h and 15.0 h, respectively, indicating that higher In loading led to a longer induction period. Noteworthily, the lifetimes of $PtIn_{0.6}/SiO_2$ and $PtIn_{0.8}/SiO_2$ were significantly increased to 61 h and

https://doi.org/10.1038/s41467-025-60153-1

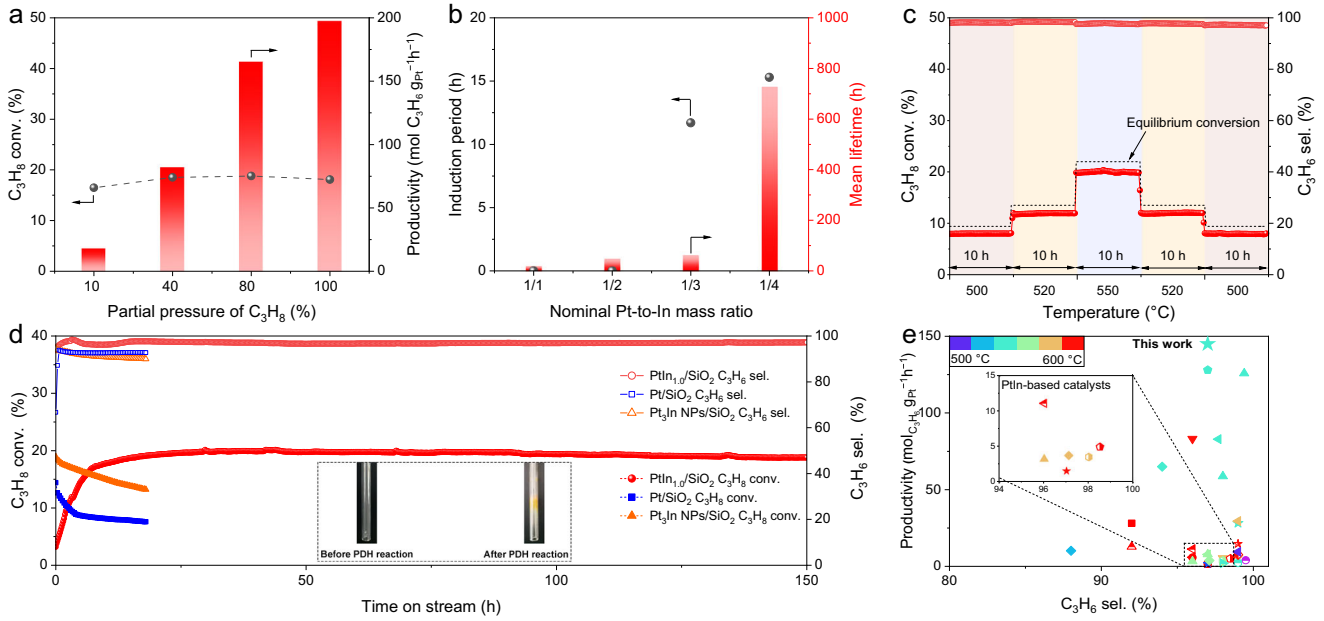

Fig. 3 | PDH performance. a PDH performance of $PtIn_{1.0}/SiO_2$ under different propane partial pressures at 550 °C. **b** PDH performance of $PtIn_{1.0}/SiO_2$ as a function of nominal Pt-to-In mass ratios. **c** PDH performance of $PtIn_{1.0}/SiO_2$ at different temperatures. **d** PDH stability test of $PtIn_{1.0}/SiO_2$, Pt/SiO_2 and Pt_3In NPs/SiO_2. Reaction condition: atmospheric pressure, WHSV = 39 h^{-1}, 550 °C, C_3H_8/H_2 = 2/1. The inset shows the bottom of the quartz tube before and after the PDH reaction. **e** C_3H_6 productivity versus C_3H_6 selectivity for the Pt-based catalysts described in this work and literature. The catalysts included here are only the best-performing ones from the articles considered.

726 h, respectively, demonstrating that increased In loading enhanced catalyst stability. For $PtIn_{1.0}/SiO_2$, C_3H_8 conversion increased constantly during 20-h TOS. Whereas further increasing the In loading to 1.5 wt% or 3.0 wt% resulted in lower overall catalytic activity, likely due to the active Pt sites being covered by excessive In^0. At 20 h, $PtIn_{1.0}/SiO_2$ exhibited the highest C_3H_6 productivity of 121 mol g_{Pt}^{-1} h^{-1} among all $PtIn_x/SiO_2$ samples. Thus, to optimize C_3H_6 productivity, the $PtIn_{1.0}/SiO_2$ sample was chosen for further evaluation.

The maximum activity of $PtIn_{1.0}/SiO_2$ was investigated by increasing the WHSV after the induction period. As a result, the C_3H_6 productivity of $PtIn_{1.0}/SiO_2$ reached a peak of 317.2 mol g_{Pt}^{-1} h^{-1} under the WHSV of 118 h^{-1} (Supplementary Fig. 14). The stability of the optimal $PtIn_{1.0}/SiO_2$ catalyst was evaluated under different temperatures after the catalytic activity reached its peak. It is worth noting that evaluating catalyst stability at equilibrium conversion should be avoided since seemingly high apparent stability can be obtained by overloading the catalyst. As shown in Fig. 3c, under the WHSV of 39 h^{-1}, the C_3H_8 conversion increased with temperature and remained steady at each stage. The C_3H_8 conversions of $PtIn_{1.0}/SiO_2$ at each stage were lower than the corresponding equilibrium conversions. After the heating and cooling processes, the C_3H_8 conversion at the final stage was completely restored to 7.9%, matching the initial stage. Therefore, the stable structure of $PtIn_{1.0}/SiO_2$ demonstrated excellent temperature tolerance, ranging from 500 to 550 °C.

To further evaluate the catalytic stability of $PtIn_{1.0}/SiO_2$, we performed the long-term PDH test. As shown in Fig. 3d, the C_3H_8 conversion of Pt/SiO_2 dropped gradually from 14.4% to 7.6% during an 18-h TOS. Concurrently, the C_3H_6 selectivity surged from 66.7% to 93.2% during the initial stage (TOS < 1 h) and remained unchanged as the PDH reaction progressed. The mean lifetime of Pt/SiO_2 was calculated as 29 h. In contrast, $PtIn_{1.0}/SiO_2$ initially exhibited a C_3H_8 conversion of 3.2%, which significantly increased to a maximum (20.1%) after 30-h TOS, corresponding to the C_3H_6 productivity of 145 mol g_{Pt}^{-1} h^{-1}. As the PDH test progressed, the C_3H_8 conversion of $PtIn_{1.0}/SiO_2$ decreased slightly to 18.8%, giving a mean lifetime of 1395 h. Meanwhile, the C_3H_6 selectivity remained as high as 97% during the 150-h test.

The coke formation on Pt/SiO_2 and $PtIn_{1.0}/SiO_2$ was assessed using thermogravimetry (TG) analysis and Raman spectroscopy. As shown in Supplementary Fig. 15, the coke formation rate on Pt/SiO_2 was calculated as 1.3 mg_{coke} g_{cat}^{-1} h^{-1} during the 18-h PDH test. In contrast, the coke formation rate on $PtIn_{1.0}/SiO_2$ during 150-h PDH test was 0.12 $mg_{coke}g_{cat}^{-1}h^{-1}$, 10.8 times lower than that of Pt/SiO_2. Furthermore, the graphitization degree of the formed coke was evaluated by Raman spectroscopy (Supplementary Fig. 16). After 18-h TOS, the I_D/I_G value for $PtIn_{1.0}/SiO_2$ was 1.88, higher than that of Pt/SiO_2 (1.78), indicating a higher degree of disorder in the formed coke. This result aligns with the TG analysis, where coke on $PtIn_{1.0}/SiO_2$ was oxidized at lower temperatures (473 °C) compared to Pt/SiO_2 (526 °C). Therefore, In^0 species effectively improve the C_3H_6 selectivity and retard the coke formation.

According to previous studies, Pt_3In intermetallic was predicted to exhibit maximal C_3H_6 productivity among Pt-based alloy catalysts[47]. We prepared SiO_2-supported Pt_3In NPs (Pt_3In NPs/SiO_2) using the colloid method to evaluate their catalytic performance[39]. XRD and XPS characterizations demonstrated the successful preparation of Pt_3In intermetallic (Supplementary Figs. 17, 18). As displayed in Fig. 3d, Pt_3In NPs/SiO_2 catalyst exhibited an initial C_3H_6 selectivity of 95%, much higher than that of Pt/SiO_2, demonstrating the effective dilution of Pt sites by In atoms. Besides, the initial C_3H_8 conversion and C_3H_6 productivity of Pt_3In NPs/SiO_2 were as high as 18.9% and 122.3 mol g_{Pt}^{-1} h^{-1}, suggesting the superior catalytic activity of Pt_3In NPs. Nevertheless, during 18-h TOS, both C_3H_8 conversion and C_3H_6 selectivity decreased constantly, resulting in a low lifetime of 42 h. We also tested the activity of $In_{1.0}/SiO_2$, which was almost inert toward PDH reaction (Supplementary Fig. 19). Thus, the high C_3H_6 productivity and C_3H_6 selectivity demonstrate the outstanding catalytic performance of $PtIn_{1.0}/SiO_2$ catalyst, which is superior to most of the state-of-the-art Pt-based catalysts (Fig. 3e and Supplementary Table S3).

https://doi.org/10.1038/s41467-025-60153-1

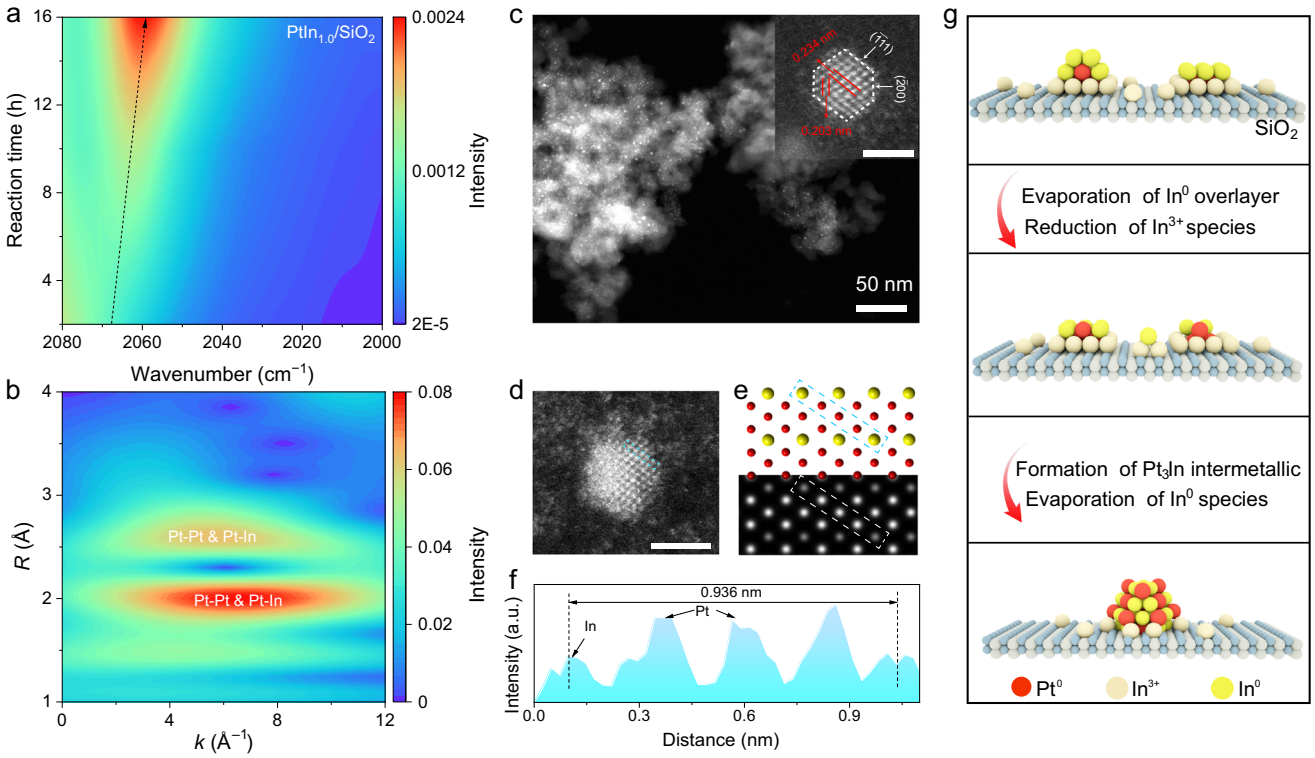

Fig. 4 | Unveiling the origin of high PDH performance. a In situ CO DRIFTS results of $PtIn_{1.0}/SiO_2$ after PDH reaction for different times. **b** Wavelet transformed EXAFS spectra of $PtIn_{1.0}/SiO_2$ after PDH reaction at the Pt L_{III}-edge. **c** HAADF-STEM image of $PtIn_{1.0}/SiO_2$ after 150-h PDH test. The scale bar of the inset was 2 nm. **d** Atomically-resolved HAADF-STEM images of individual PtIn NPs. **e** Corresponding simulated HAADF-STEM images and atomic models of Pt_3In NPs along [011] zone axis. **f** The extracted line profiles along directions in (**d**). **g** The dynamic evolution of $PtIn_{1.0}/SiO_2$ catalyst during the induction period of PDH reaction. The red, primrose, and yellow balls stand for Pt^0, In^{3+}, and In^0 species, respectively.

Catalyst dynamics during PDH reaction

Despite numerous studies identifying distinct PtIn alloy phases as potential active sites, most PtIn-based catalysts exhibited notably inferior catalytic activity, as illustrated in Fig. 3e. The most effective PtIn alloy phase for the PDH reaction is still under debate, primarily due to an insufficient understanding of the dynamic evolution of PtIn-based catalysts during the PDH reaction. Two critical knowledge gaps persist: first, the existence of In^0 overlayer in the reduced sample remains contentious, with no established methodology for its selective removal. Second, the characterization of PtIn-based catalysts after PDH reaction remains inadequately explored. While previous reports have noted similar induction periods in catalytic behavior[39,49], atomic-level insights into the dynamic evolution of active sites are conspicuously absent. Thus, investigation of the dynamic evolution of PtIn alloy is of crucial importance for the identification of real active sites, thus obtaining a high-performance catalyst.

The compositional change of $PtIn_{1.0}/SiO_2$ during PDH reaction was investigated using a series of spectroscopic characterizations. After a 150-h PDH test, a noticeable yellow substance was observed at the bottom of the quartz tube (insets of Fig. 3d). The Pt-to-In mass ratio of the above substance was determined as 1 / 5400, given by ICP-MS measurements. We further detected the Pt and In loading of spent catalysts. After the stability test and ICP-MS measurements twice, the mass ratio of Pt-to-In was 0.52 and 0.43, averaging 0.47, suggesting that a stable catalyst composition was achieved after the induction period. Due to its low melting point and heat of vaporization, metallic In^0 easily melts and evaporates at high temperatures. In comparison, the evaporation of In^{3+} species is difficult due to the high melting point of In_2O_3 (~ 2000 °C)[50]. Thus, given that only 2.8% of In^0 species were present in the reduced samples, we deduced that In^{3+} species on the SiO_2 support were continually reduced and evaporated during the PDH reaction, resulting in a substantial loss of In species (Supplementary Fig. 2). As previously discussed, the PtIn alloy was covered by an In^0 overlayer (Fig. 1f). Hence, we infer that the evaporation of In^0 overlayer leads to the induction period of $PtIn_{1.0}/SiO_2$ catalyst.

In situ CO DRIFTS measurements were conducted to verify the above hypothesis. As shown in Supplementary Fig. 20, after catalyzing PDH reaction in the infrared cell at 550 °C for different durations, Pt/SiO_2 exhibited an unchanged adsorption peak at 2,066 cm^{-1}, the same as the reduced sample (Supplementary Fig. 3). However, the integral intensity of adsorption peaks decreased constantly, suggesting the continuous sintering of Pt sites. Figure 4a and Supplementary Fig. 21 present the CO DRIFTS results of $PtIn_{1.0}/SiO_2$. With the proceeding of the PDH reaction, the adsorption peak gradually red-shifted from 2064 to 2057 cm^{-1}. The increased electron density in the Pt 5*d* orbital also facilitated the desorption of C_3H_6 and thus higher C_3H_6 selectivity[35]. Meanwhile, the increase in the integral intensity of corresponding peaks suggests that the surface Pt sites were gradually exposed, attributing to the evaporation of the In^0 overlayer.

To further investigate the characteristics of In^0 evaporation, we studied the effect of gas components. $In_{1.0}/SiO_2$ was treated under 10% H_2/Ar, 10% C_3H_6/Ar, and 10% C_3H_8/Ar at 550 °C for 10 h in the fixed-bed reactor, respectively. As a result, under 10% C_3H_6/Ar, the amount of evaporated In^0 species was 10 times higher than that under 10% H_2/Ar or 10% C_3H_8/Ar (Supplementary Fig. 22). The above results indicate that a C_3H_6 atmosphere is capable of inducing the evaporation of In^0 species. Noteworthily, a high partial pressure of C_3H_6 is indispensable, since no induction period was observed for $PtIn_{1.0}/SiO_2$ during the PDH reaction under 10% C_3H_8/Ar, in which the partial pressure of C_3H_6 was calculated as only 1.5% (Supplementary Fig. 11). Thus, C_3H_6 gas with

high partial pressure played a decisive role in the evaporation of In^0 species. To further investigate the factors affecting the time required for the In^0 evaporation, we systematically decreased the catalyst mass. $PtIn_{1.0}/SiO_2$ samples ranging from 120 to 30 mg were used, and the related WHSVs were 13 to 52 h^{-1}. A clear trend emerged that lower catalyst mass corresponded to a shorter induction period (Supplementary Figs. 23, 24). Combined with the data in Supplementary Fig. 13, these results suggest that the total amount of In^0 present in the catalyst bed dictates the duration of the induction period.

In situ synchrotron-based vacuum ultraviolet photoionization mass spectrometry (SVUV-PIMS) was further conducted to study the evaporation of In^0 species on SiO_2 support. A photon energy of 9.5 eV was chosen to ionize In, while the C_3H_6 molecule was not able to be ionized. When $In_{1.0}/SiO_2$ was exposed to 10% H_2/Ar atmosphere, characteristic signals of In were absent in the temperatures range of 550–800 °C, indicating that In species evaporated from $In_{1.0}/SiO_2$ was ignorable (Supplementary Fig. 25a). In comparison, under 10% C_3H_6/Ar, characteristic signals of In isotopes represented by mass/charge = 114.9 and 112.9 were observed when exposing $In_{1.0}/SiO_2$ at approximately 650 °C (Supplementary Fig. 25b). The intensity of In signals significantly increased when the temperature increased to 800 °C, suggesting that high temperatures also promote the evaporation of In species. Notably, due to the low gas pressure (2 Torr) and resultant low C_3H_6 partial pressure, the promoting effect of C_3H_6 on the evaporation of In species was weakened. Hence, the temperature of the gas phase In^0 species detected by SVUV-PIMS was higher than that in the fixed-bed reactor. We conclude that both the high partial pressure of C_3H_6 and high temperatures are essential for inducing the evaporation of In^0 species.

The final structure of the spent $PtIn_{1.0}/SiO_2$ catalyst (after the PDH stability test) was studied to uncover the origin of its high catalytic performance. XANES and EXAFS measurements were employed to characterize the electronic structure of the spent $PtIn_{1.0}/SiO_2$ catalyst. As depicted in Supplementary Fig. 26, the XANES spectra at the Pt L_{III}-edge showed that, compared to the reduced sample, the spent $PtIn_{1.0}/SiO_2$ exhibited a decrease in absorption edge and white line intensity. This indicated that Pt species were further reduced during the PDH test, consistent with the CO-DRIFTS results (Fig. 4a). The EXAFS results showed the Pt–Pt CN of 4.5 and Pt–In CN of 2.3 (Fig. 4b, Supplementary Fig. 26 and Table S2). The bonding distance of Pt–Pt and Pt–In was 2.58 Å and 2.63 Å, respectively, indicative of the small size of PtIn alloy. Noteworthily, the CN ratio of Pt–Pt and Pt–In in $PtIn_{1.0}/SiO_2$ was calculated as 2 (4.5 / 2.3), in good agreement with the theoretical value of Pt_3In (8 / 4) at a bonding distance of 2.82 Å. Hence, we deduced that the PtIn clusters evolved into Pt_3 In intermetallic during the PDH stability test.

Atomically resolved HAADF-STEM characterization was further performed to corroborate the aforementioned deduction. As shown in Fig. 4c and Supplementary Fig. 27, the spent $PtIn_{1.0}/SiO_2$ catalyst exhibited as NPs with an ordered arrangement. In addition, a large amount of residual atomically dispersed In^{3+} species were present on SiO_2 support. HAADF-STEM observations with a broad vision showed a uniform distribution with an average size of 1.3 nm. Besides, NPs larger than 2.3 nm were absent, suggesting the exceptional sintering resistance of $PtIn_{1.0}/SiO_2$. We further analyzed the structure of individual NPs by measuring the interplanar distances. For NPs in the spent Pt/SiO_2 sample, the Fast Fourier Transform (FFT) pattern showed a typical face-centered cubic crystal structure under the [011] zone axis (Supplementary Fig. 28). The *d*-spacing of the {111} plane was measured as 0.223 nm, closely aligning with the theoretic value. In comparison, significant lattice expansion was observed for $PtIn_{1.0}/SiO_2$. Under the [011] zone axis, the *d*-spacing of {111} and {200} planes were measured to be 0.234 nm and 0.203 nm, respectively (Fig. 4c and Supplementary Fig. 27). The expanded lattice spacing was in line with that of the Pt_3In intermetallic under the [011] zone axis. The structure of Pt_3In intermetallic was verified by distinguishing elements in an individual NP according to their Z-contrast (Fig. 4d–f). Along the direction of the rectangle in Fig. 4d, an oscillation of intensity was observed, attributed to the difference in Z-contrast between Pt and In. Under the [011] zone axis, the oscillation of intensity corresponded with the models and STEM simulations of Pt_3In intermetallic. Besides, the *d*-spacing of {111} plane was estimated to be 0.234 nm, consistent with the results in Fig. 4c. Thus, for the spent $PtIn_{1.0}/SiO_2$, we identified Pt_3In intermetallic, an ordered $L1_2$ structure with alternating stack of mixed Pt/In columns and Pt columns along the [011] zone axis. Combining the HAADF-STEM observations and EXAFS results, we conclude that during the PDH reaction, PtIn clusters gradually evolved into ultrafine Pt_3In intermetallic (averaging 1.3 nm), which served as the real active site in the PDH reaction (Fig. 4g).

To demonstrate the necessity of constructing ultrafine Pt_3In intermetallic via dynamic evolution, spent Pt/SiO_2 and Pt_3In NPs/SiO_2 catalysts were characterized. For Pt/SiO_2, the average size increased from 2.5 to 3.4 nm, indicating that Pt NPs underwent continuous sintering during the PDH test (Supplementary Fig. 28). For Pt_3In NPs/SiO_2, XPS results in Supplementary Fig. 18 showed that only metallic Pt and In species were present in Pt_3In NPs/SiO_2. HAADF-STEM images in Supplementary Fig. 29 indicated that Pt_3In intermetallic also underwent severe sintering, suggesting that In^0 species could not prevent the aggregation of active Pt sites. In contrast, those In^{3+} species at the interface of Pt_3In intermetallic and SiO_2 support served as nano-islands, effectively frustrating the sintering of the evolved Pt_3In intermetallic (Supplementary Fig. 27). The quick deactivation of $PtIn_{0.6}/SiO_2$ and $PtIn_{0.8}/SiO_2$ was ascribed to In^{3+} species being not enough to prevent the sintering of PtIn clusters. To verify the above hypothesis, we characterized the reduced and spent $PtIn_{0.8}/SiO_2$. As shown in Supplementary Fig. 30, the average size of PtIn clusters increased from 1.6 nm to 2.7 nm, indicating that slight sintering occurred during PDH reaction. Thus, sufficient In^{3+} species play a crucial role in the high catalytic stability of $PtIn_{1.0}/SiO_2$. Compared with the direct synthesis of Pt_3In intermetallic with high catalytic activity, the construction of active Pt sites through dynamic evolution was demonstrated to be more effective.

Moreover, the evolved Pt_3In intermetallic exhibited an ultrafine nature (averaging 1.3 nm), smaller than reduced Pt/SiO_2. This suggests that dynamic evolution during PDH serves as an effective synthetic strategy for engineering ultrafine bimetallic alloy nanoparticles, which outperform their monometallic counterparts in catalytic performance across various reactions. To experimentally validate this hypothesis, we systematically evaluated the catalytic performance of spent $PtIn_{1.0}/SiO_2$-PDH in CO_2 hydrogenation (Supplementary Fig. 31). For Pt/SiO_2, CO_2 conversion increased from 1.8% to 28.0% as temperature rose from 300 to 500 °C. $In_{1.0}/SiO_2$ exhibited low catalytic activity and poor selectivity for CO. The catalytic activity of untreated $PtIn_{1.0}/SiO_2$ was significantly lower than that of Pt/SiO_2 due to the coverage of an In^0 overlayer. Notably, after catalyzing PDH reaction under 67%C_3H_8/33%H_2 for 30 h, the catalytic activity of spent $PtIn_{1.0}/SiO_2$-PDH improved substantially. At 500 °C, the spent $PtIn_{1.0}/SiO_2$-PDH sample exhibited a CO_2 conversion of 41.0%, representing 3.0-fold and 1.4-fold enhancements over reduced $PtIn_{1.0}/SiO_2$ (13.5%) and Pt/SiO_2 (28.0%), respectively. These findings conclusively demonstrate that the in situ removal of In^0 overlayer during PDH activation can be further utilized to optimize the catalytic performance in CO_2 hydrogenation. By tailoring the active metal component, this strategy can be extended to other metal-indium alloy catalysts for a broad range of reactions.

Discussion

In heterogeneous catalysis, gas-phase reaction environments drive profound dynamic evolution of catalysts that critically determine catalytic performance. In this work, we unveiled the dynamic evolution of $PtIn_{1.0}/SiO_2$ catalyst during PDH reaction at the atomic scale.

Upon H_2 reduction, disordered PtIn alloy clusters with an In^0 overlayer were formed, with large quantities of In^{3+} species still present on SiO_2 support. In^{3+} species effectively frustrated the sintering of PtIn clusters, while In^0 species diluted Pt-Pt ensembles to improve the propylene selectivity. Propylene molecules were demonstrated to induce the evaporation of the In^0 overlayer and the exposure of active Pt sites, leading to an observable induction period. As a result, PtIn clusters evolved into ultrafine Pt_3In intermetallic (average size ~1.3 nm), exhibiting a C_3H_6 productivity of 145 mol g_{Pt}^{-1} h^{-1} and mean lifetime of approximately 1400 h. These findings highlight the importance of product molecules in the dynamic evolution of active sites, offering a new perspective for the rational design of high-performance PDH catalysts.

Methods

Synthesis of $In_{1.0}/SiO_2$

500 mg of SiO_2 was dispersed in 30 mL of 10 mM NaOH aqueous solution at room temperature. The solution was stirred for 30 min. Subsequently, the mixture was centrifugated and washed with DI water twice. SiO_2 was re-dispersed in 20 mL of DI water, giving a pH of approximately 9.0. Then, 13.1 mg of $In(NO_3)_3{\cdot}xH_2O$ was added to the mixture, and the pH slightly decreased to 8.7, suggesting that most of the In^{3+} cations were adsorbed onto SiO_2 before hydrolysis. The mixture was stirred for 10 min. The sample was collected by vacuum filtration and dried at 60 °C in an oven overnight. Finally, the powder was calcined at 300 °C for 1 h. The loading of In on SiO_2 was determined as 0.9 wt% by ICP-MS measurement. For In_x/SiO_2 (x = 0.2, 0.4, 0.6, 0.8, 1.5, 3.0), the synthetic procedure was the same as that of $In_{1.0}/SiO_2$, except for varying the amount of $In(NO_3)_3{\cdot}xH_2O$.

Synthesis of $PtIn_{1.0}/SiO_2$

The synthetic procedure of $PtIn_{1.0}/SiO_2$ follows a SEA method. In a typical synthesis, 300 mg of $In_{1.0}/SiO_2$ was immersed in 100 mL of DI water and sonicated. The pH of the solution was adjusted to 10–11 by adding 2 mL of 2 M ammonia solution. Simultaneously, 3.9 μmol of $Pt(NH_3)_4(NO_3)_2$ was dissolved in 25 mL of DI water to obtain the precursor solution. Under vigorous stirring, 20 mL of Pt precursor solution was slowly pumped into the aqueous solution containing $In_{1.0}/SiO_2$ in 30 min. After being stirred for another 30 min, vacuum filtration was applied to collect the sample, which was dried at 60 °C in an oven overnight. The loading of Pt on $In_{1.0}/SiO_2$ was determined as 0.12 wt% by ICP-MS measurement. The synthetic procedure $PtIn_x/SiO_2$ (x = 0.2, 0.4, 0.6, 0.8, 1.5) was the same as that of $PtIn_{1.0}/SiO_2$, except for changing $In_{1.0}/SiO_2$ to In_x/SiO_2.

Catalytic reaction

The PDH test was performed in a vertical, quartz fixed-bed reactor with an internal diameter of 7 mm under atmospheric pressure. Generally, 40 mg of catalysts, diluted with 960 mg quartz sand, were packed inside the quartz tube. The catalyst was reduced in 10% H_2/Ar at 600 °C for 1 h. Subsequently, the temperature was decreased to 550 °C. The WHSV was calculated based on the ratio of the mass flow rate of C_3H_8 and the mass of the catalyst. Effluent gas was analyzed by Agilent 8860 chromatography with an FID detector. For all tests, C_3H_8, C_3H_6, C_2H_6, C_2H_4, and CH_4 were detected. C_3H_8 conversion, C_3H_6 selectivity, and carbon balance were calculated via an external standard method based on Eqs. 2, 3, respectively. Carbon balance was calculated according to the following Eq. 4, giving a value between 95% and 105% for all tests.

$$C_3H_8\text{conversion} = 1 - \frac{[C_3H_8]_{out}}{[C_3H_8]_{out} + [C_3H_6]_{out} + \frac{2}{3}[C_2H_6]_{out} + \frac{2}{3}[C_2H_4]_{out} + \frac{1}{3}[CH_4]_{out}} \times 100\% \quad (2)$$

$$C_3H_6\text{selectivity} = \frac{[C_3H_6]_{out}}{[C_3H_6]_{out} + \frac{2}{3}[C_2H_6]_{out} + \frac{2}{3}[C_2H_4]_{out} + \frac{1}{3}[CH_4]_{out}} \times 100\% \quad (3)$$

$$\text{Carbon balance} = \frac{[C_3H_8]_{out} + [C_3H_6]_{out} + \frac{2}{3}[C_2H_6]_{out} + \frac{2}{3}[C_2H_4]_{out} + \frac{1}{3}[CH_4]_{out}}{[C_3H_8]_{in}} \times 100\% \quad (4)$$

SVUV-PIMS measurements

SVUV-PIMS measurements were carried out at the combustion beamline (BL03U) of the National Synchrotron Radiation Laboratory at Hefei, China. $In_{1.0}/SiO_2$ was packed in a quartz reactor with a nozzle size of approximately 0.1 mm, which was connected to an online SVUV-PIMS spectrometer. Catalysts were firstly reduced in H_2 flow (H_2:Ar = 1:9) with a total flow rate of 40 mL min^{-1} at 600 °C for 1 h and cooled down to 550 °C. Subsequently, the gas was kept unchanged or switched to 10% C_3H_6/Ar. Data were recorded by MS from 550 °C to 800 °C. The photon energy was 9.5 eV, and the pressure was controlled at 2 Torr.

Simulations of HAADF-STEM images

The HAADF-STEM simulations were conducted with QSTEM software[51]. A structure model containing a PtIn cluster and SiO_2 support was established according to the experimental results. The structure model was imported into QSTEM software to generate an HAADF-STEM image. To verify the rationality of our structure model, 3D intensity distribution maps were derived and compared with the corresponding experimental ones.

Data availability

All data supporting the findings of this study are available within the main text, figures and Supplementary Information, or from the corresponding authors upon request. Source data are provided in this paper.

References

1. Hu, S. L. & Li, W.-X. Sabatier principle of metal-support interaction for design of ultrastable metal nanocatalysts. *Science* **374**, 1360–1365 (2021).
2. Somorjai, G. A., McCrea, K. R. & Zhu, J. Active sites in heterogeneous catalysis: development of molecular concepts and future challenges. *Top. Catal.* **18**, 157–162 (2002).
3. Gates, B. C., Katz, A. & Liu, J. Nested metal catalysts: metal atoms and clusters stabilized byconfinement with accessibility on supports. *Precis. Chem.* **1**, 3–13 (2023).
4. Chavez, S. et al. Studying, promoting, exploiting, and predicting catalyst dynamics: the next frontier in heterogeneous catalysis. *J. Phy. Chem. C.* **127**, 2127–2146 (2023).
5. Corma, A. Heterogeneous catalysis: understanding for designing, and designing for applications. *Angew. Chem. Int. Ed.* **128**, 6218–6219 (2016).
6. Duan, M. et al. Reconstruction of supported metal nanoparticles in reaction conditions. *Angew. Chem. Int. Ed.* **130**, 6574–6579 (2018).
7. Nagai, Y. et al. In situ redispersion of Platinum autoexhaust catalysts: an on-line approach to increasing catalyst lifetimes? *Angew. Chem. Int. Ed.* **47**, 9303–9306 (2008).
8. Dai, Y., Lu, P., Cao, Z., Campbell, C. T. & Xia, Y. The physical chemistry and materials science behind sinter-resistant catalysts. *Chem. Soc. Rev.* **47**, 4314 (2018).
9. Yuan, W. et al. Direct in situ TEM visualization and insight into the facet-dependent sintering behaviors of Gold on TiO_2. *Angew. Chem. Int. Ed.* **130**, 17069–17073 (2018).
10. Yang, C. et al. Surface faceting and reconstruction of ceria nanoparticles. *Angew. Chem. Int. Ed.* **56**, 375–379 (2016).

11. Zhu, J. et al. Dynamic structural evolution of iron catalysts involving competitive oxidation and carburization during CO_2 hydrogenation. *Sci. Adv.* **8**, eabm3629 (2022).
12. Avanesian, T. et al. Quantitative and atomic-scale view of CO-induced Pt nanoparticle surface reconstruction at saturation coverage via DFT calculations coupled with in Situ TEM and IR. *J. Am. Chem. Soc.* **139**, 4551–4558 (2017).
13. Yan, G. et al. Reaction product-driven restructuring and assisted stabilization of a highly dispersed Rh-on-ceria catalyst. *Nat. Catal.* **5**, 119–127 (2022).
14. Luo, L., Engelhard, M. H., Shao, Y. & Wang, C. Revealing the dynamics of platinum nanoparticle catalysts on carbon in oxygen and water using environmental TEM. *ACS Catal.* **7**, 7658–7664 (2017).
15. Tao, F. Reaction-driven restructuring of Rh-Pd and Pt-Pd core-shell nanoparticles. *Science* **32**, 932–934 (2008).
16. Zhang, Z., Zandkarimi, B. & Alexandrova, A. N. Ensembles of metastable states govern heterogeneous catalysis on dynamic interfaces. *Acc. Chem. Res.* **53**, 447–458 (2020).
17. Chen, S. et al. Propane dehydrogenation: catalyst development, new chemistry, and emerging technologies. *Chem. Soc. Rev.* **50**, 3315–3354 (2021).
18. Yuan, Y., Huang, E., Hwang, S., Liu, P. & Chen, J. G. Confining platinum clusters in indium-modified ZSM-5 zeolite to promote propane dehydrogenation. *Nat. Commun.* **15**, 6529 (2024).
19. Wang, P. et al. Enhanced PtIn catalyst via Ce-assisted confinement effect in propane dehydrogenation. *ACS Catal.* **14**, 8116–8129 (2024).
20. Luo, L. et al. Close intimacy between PtIn clusters and zeolite channels for ultrastability toward propane dehydrogenation. *Nano Lett.* **24**, 7236–7243 (2024).
21. Liu, L. et al. Structural modulation and direct measurement of subnanometric bimetallic PtSn clusters confined in zeolites. *Nat. Catal.* **3**, 628–638 (2020).
22. Festa, G. et al. Support screening to shape propane dehydrogenation SnPt-based catalysts. *Ind. Eng. Chem. Res.* **63**, 16269–16284 (2024).
23. Festa, G., Contaldo, P., Martino, M., Meloni, E. & Palma, V. Modeling the selectivity of hydrotalcite-based catalyst in the propane dehydrogenation reaction. *Ind. Eng. Chem. Res.* **62**, 16622–16637 (2023).
24. Sun, G. et al. Breaking the scaling relationship via thermally stable Pt/Cu single atom alloys for catalytic dehydrogenation. *Nat. Commun.* **9**, 4454 (2018).
25. Marcinkowski, M. D. et al. Pt/Cu single-atom alloys as coke-resistant catalysts for efficient C–H activation. *Nat. Chem.* **10**, 325–332 (2018).
26. Searles, K. et al. Highly productive propane dehydrogenation catalyst using silica-supported Ga–Pt nanoparticles generated from single-sites. *J. Am. Chem. Soc.* **140**, 11674–11679 (2018).
27. Qi, L. et al. Propane dehydrogenation catalyzed by isolated Pt atoms in ≡SiOZn–OH nests in dealuminated zeolite beta. *J. Am. Chem. Soc.* **143**, 21364–21378 (2021).
28. Sun, Q. et al. Subnanometer bimetallic platinum–zinc clusters in zeolites for propane dehydrogenation. *Angew. Chem. Int. Ed.* **59**, 19450–19459 (2020).
29. Xie, L. et al. Optimizing zeolite stabilized Pt-Zn catalysts for propane dehydrogenation. *J. Energy Chem.* **57**, 92–98 (2021).
30. Luo, L. et al. A promoted $PtFe/SiO_2$ catalyst with low Pt concentration for propane dehydrogenation. *Catal. Sci. Technol.* **13**, 3395–3402 (2023).
31. Nakaya, Y. et al. High-entropy intermetallics serve ultrastable single-atom Pt for propane dehydrogenation. *J. Am. Chem. Soc.* **144**, 15944–15953 (2022).
32. Wu, Z. et al. Changes in catalytic and adsorptive properties of 2 nm Pt_3Mn nanoparticles by subsurface atoms. *J. Am. Chem. Soc.* **140**, 14870–14877 (2018).
33. Ryoo, R. et al. Rare-earth–platinum alloy nanoparticles in mesoporous zeolite for catalysis. *Nature* **585**, 221–224 (2020).
34. Ma, Y. et al. Germanium-enriched double-four-membered-ring units inducing zeolite-confined subnanometric Pt clusters for efficient propane dehydrogenation. *Nat. Catal.* **6**, 506–518 (2023).
35. Chang, X. et al. Designing single-site alloy catalysts using a degree-of-isolation descriptor. *Nat. Nanotechnol.* **18**, 611–616 (2023).
36. Tian, J. et al. Non-classical deactivation mechanism in a supported intermetallic catalyst for propane dehydrogenation. *Angew. Chem. Int. Ed.* **136**, e202409556 (2024).
37. Kosmulski, M. Isoelectric points and points of zero charge of metal (hydr)oxides: 50 years after Parks' review. *Adv. Colloid Interface Sci.* **238**, 1–61 (2016).
38. Wong, A., Liu, Q., Griffin, S., Nicholls, A. & Regalbuto, J. R. Synthesis of ultrasmall, homogeneously alloyed, bimetallic nanoparticles on silica supports. *Science* **358**, 1427–1430 (2017).
39. Escorcia, N. J., LiBretto, N. J., Miller, J. T. & Li, C. W. Colloidal synthesis of well-defined bimetallic nanoparticles for nonoxidative alkane dehydrogenation. *ACS Catal.* **10**, 9813–9823 (2020).
40. Uemura, Y. et al. Core–shell phase separation and structural transformation of Pt_3Sn alloy nanoparticles supported on γ-Al_2O_3 in the reduction and oxidation processes characterized by in situ time-resolved XAFS. *J. Phys. Chem. C.* **115**, 5823–5833 (2011).
41. Bus, E. & van Bokhoven, J. A. Electronic and geometric structures of supported platinum, gold, and platinum-gold catalysts. *J. Phys. Chem. C.* **111**, 9761–9768 (2007).
42. Wegener, E. C. et al. Structure and reactivity of Pt–In intermetallic alloy nanoparticles: highly selective catalysts for ethane dehydrogenation. *Catal. Today* **299**, 146–153 (2018).
43. Tyson, W. R. Surface free energies of solid metals: estimation from liquid surface tension measurements. *Surf. Sci.* **62**, 267–276 (1997).
44. Zhou, C. et al. Understanding and harnessing nanoscale immiscibility in Ru–In alloys for selective CO_2 hydrogenation. *J. Am. Chem. Soc.* **146**, 19986–19997 (2024).
45. Zhou, T., et al. Ultrafine metal nanoparticles isolated on oxide nanoislands as exceptional sintering-resistant catalysts. *Nat. Mater.* https://doi.org/10.1038/s41563-025-02134-9 (2025).
46. Larsson, M., Andersson, B., Hulten, M. & Blekkan, E. A. The effect of reaction conditions and time on stream on the coke formed during propane dehydrogenation. *J. Catal.* **164**, 44–53 (1996).
47. Zha, S. et al. Identification of Pt-based catalysts for propane dehydrogenation via a probability analysis. *Chem. Sci.* **9**, 3925–3931 (2018).
48. Octave, L. *Chemical Reaction Engineering, 3rd Edition* (Wiley, New York, 1999).
49. Zeng, L. et al. Stable anchoring of single rhodium atoms by indium in zeolite alkane dehydrogenation catalysts. *Science* **383**, 998–1004 (2024).
50. Rumble, J. R. *CRC Handbook of Chemistry and Physics* (CRC Press/Taylor & Francis, 2021).
51. Koch, C. *Determination of Core Structure Periodicity and Point Defect Density Along Dislocations*. (Arizona State University, 2002).

Acknowledgements

J. Zeng acknowledges the National Key Research and Development Program of China (2021YFA1500500), CAS Project for Young Scientists in Basic Research (YSBR-051), National Science Fund for Distinguished Young Scholars (21925204), NSFC (22525021, 22221003, 22250007,

22361162655), the Science and Technology Development Fund (FDCT) of Macao S.A.R (0070/2023/AFJ), Fundamental Research Funds for the Central Universities, Joint Fund of Yulin University and the Dalian National Laboratory for Clean Energy (YLU-DNL Fund 2022012), State Key Laboratory of Catalysis (2024SKL-A-011), International Partnership Program of Chinese Academy of Sciences (123GJHZ2022101GC) and the New Cornerstone Science Foundation through the XPLORER PRIZE. X.L. acknowledges the NSFC (22475030, 22201272) and Central Government Funds of Guiding Local Scientific and Technological Development for Sichuan Province (2024ZYD0152), Sichuan Science and Technology Program (2024NSFSC1107). H.Y. acknowledges the NSFC (22302185), the Fundamental Research Funds for the Central Universities (WK9990000167), Young Elite Scientists Sponsorship Program by CAST (2022QNRC001), and Anhui Natural Science Foundation for Young Scholars (2308085QB53). W.W. acknowledges the NSFC (22204158). This work was partially carried out at the Instruments Center for Physical Science, University of Science and Technology of China. We thank the BL11B beamlines at Shanghai Synchrotron Radiation Facility and the 1W1B beamline at Beijing Synchrotron Radiation Facility for the XAFS measurements.

Author contributions

T.Z. and H.Y. equally contributed to this work. T.Z., X.L., and J.Z. came up with the idea and designed the study. T.Z., H.Y., X.L., W.L., W.Z., and H.H. synthesized catalysts and conducted structural characterizations. S.H. conducted the HAADF-STEM simulations. R.W. processed the XAFS results. T.Z., T.X., C.L., and Y.P. conducted the SVUV-PIMS experiments. T.Z., L.L., and X.Z. conducted the XPS measurements with Ar^+ sputtering. L.Z. and W.W. provided valuable suggestions on the research project. T.Z., H.Y., and X.L. analyzed the data and co-wrote the paper. J.Z. and X.L. supervised the work. All authors discussed the results and commented on the manuscript.

Competing interests

The authors declare no competing interests.

Additional information

Supplementary information The online version contains supplementary material available at https://doi.org/10.1038/s41467-025-60153-1.

Correspondence and requests for materials should be addressed to Jie Zeng or Xu Li.

Peer review information *Nature Communications* thanks Raquel Poterla and the other anonymous reviewer(s) for their contribution to the peer review of this work. A peer review file is available.